Formation and sink of glyoxal and methylglyoxal in a polluted subtropical environment: observation-based photochemical analysis and impact evaluation

Zhenhao Ling[1], Qianqian Xie[2], Zhe Wang[3,4]*, Tao Wang[5], Hai Guo[5], Xuemei Wang[2,4]*

[1.] School of Atmospheric Sciences, Guangdong Province Key Laboratory for Climate Change and Natural Disaster Studies, Sun Yat-sen University and Southern Marine Science and Engineering Guangdong Laboratory (Zhuhai), Zhuhai, China

[2.] Institute for Environmental and Climate Research, Jinan University, Guangzhou, China

[3.] Division of Environment and Sustainability, The Hong Kong University of Science and Technology, Hong Kong, China

[4.] Guangdong-Hongkong-Macau Joint Laboratory of Collaborative Innovation for Environmental Quality, Guangzhou, China

[5.] Department of Civil and Environmental Engineering, Hong Kong Polytechnic University, Hong Kong, China

*Correspondence: Zhe Wang (z.wang@ust.hk) and Xuemei Wang (eciwxm@jnu.edu.cn)

Abstract

The dicarbonyls, glyoxal (Gly) and methylglyoxal (Mgly) have been recognized as important precursors of secondary organic aerosols (SOAs) through the atmospheric heterogeneous process. In this study, field measurement was conducted at a receptor site in the Pearl River Delta (PRD) region in south China, and an observation based photochemical box model was subsequently applied to investigate the production and evolution of Gly and Mgly as well as their contributions to SOA formation. The model was coupled with a detailed gas-phase oxidation mechanism of volatile organic compounds (VOCs) (*i.e.,* MCM v3.2), heterogeneous processes of Gly and Mgly (*i.e.,* reversible partitioning in aqueous phase, irreversible volume reactions and irreversible surface uptake processes), and the gas-particle partitioning of oxidation products. The results suggested that without considering the heterogeneous processes of Gly and Mgly on aerosol surfaces, the model would overpredict the mixing ratios of Gly and Mgly by factors of 3.3 and 3.5 compared to the observed levels. The agreement between observation and simulation improved significantly when the irreversible uptake and the reversible partitioning were incorporated into the model, which in total both contributed ~62% to the destruction of Gly and Mgly during daytime, respectively. Further analysis on the photochemical budget of Gly and Mgly showed that the oxidation of aromatics by the OH radical was the major pathway producing Gly and Mgly, followed by

degradation of alkynes and alkenes. Furthermore, based on the improved model mechanism, the contributions of VOCs oxidation to SOA formed from gas-particle partitioning (SOA_{gp}) and from heterogeneous processes of Gly and Mgly (SOA_{het}) were also quantified. It was found that *o*-xylene was the most significant contributor to SOA_{gp} formation (~29%), while *m,p*-xylene and toluene made dominant contributions to SOA_{het} formation. Overall, the heterogeneous processes of Gly and Mgly can explain ~21% of SOA mass in the PRD region. The results of this study demonstrated the important roles of heterogeneous processes of Gly and Mgly in SOA formation, and highlighted the need for a better understanding of the evolution of intermediate oxidation products.

1. Introduction

Organic aerosols (OAs) are important components of atmospheric aerosols, with important impacts on radiation balance, air quality, atmospheric oxidative capacity, and climate change (Zhu et al., 2011; Carlton et al., 2009; Hoyle et al., 2009). In addition to the primary organic components (primary OA, POA) directly emitted from various sources in the particulate form, a large fraction of OAs are secondarily produced (SOA) through the aging of POAs, and through complex homogenous/heterogeneous reactions of volatile or semi-volatile organic compounds (VOCs, SVOCs) (Jimenez et al., 2009; Steinfeld and Jeffrey, 1998). SOA has frequently been observed to dominate the OA in many regions, particularly during severe haze pollution events (Guo et al., 2012; Zhang et al., 2017). However, the characteristics of SOAs are still poorly understood because of their complicated formation mechanisms, various chemical compositions, and multitude of precursors from diverse emissions, thus making SOAs an important research topic in the field of the atmospheric environment.

In addition to primary precursors including isoprene, terpene and aromatic hydrocarbons, glyoxal (Gly) and methylglyoxal (Mgly) have been recognized to be of critical importance to SOA formation, especially through heterogeneous and multiphase processes, in many laboratory and model studies (Waxman, et al., 2013, 2015; McNeill

67   et al., 2015; De Haan et al., 2009; Fu et al., 2008). Many efforts have been made to

68   investigate the sources, evolution of Gly and Mgly and their contributions to SOA

69   (Benavent et al., 2019; Zhang et al., 2016; Sumner et al., 2014; DiGangi et al., 2012;

70   Stavarakou et al., 2009). For example, Li et al (2015) constructed a Master Chemical

71   Mechanism with an equilibrium partitioning module and coupled it in a Community

72   Air Quality Model (CMAQ) to predict the regional concentrations of SOA from VOCs

73   in the eastern United States (U.S). It was found that those SOA formed from Gly and

74   Mgly were accounted for more than 35% of total SOA. Similarly, Ying et al. (2015)

75   used a modified SAPRC-11 (S11) photochemical mechanism, considering the surface-

76   controlled reactive uptake of Gly and Mgly, and incorporated the mechanism in the

77   CMAQ model to simulate ambient SOA concentrations during summer in the eastern

78   U.S. The results showed that the uptake of Gly and Mgly resulted in the significant

79   improvement in predicated SOA concentration, and the aerosol surface uptake of

80   isoprene-generated Gly, Mgly and epoxydiol accounted for more than 45% of total SOA.

81   As two smallest dicarbonyl compounds, the sources of Gly and Mgly are

82   complicated. It has been well documented that Gly and Mgly have limited primary

83   sources except biomass burning and biofuel combustion (Grosjean et al., 2001; Zhang

84   et al., 2016). Furthermore, the primary emissions of Gly and Mgly were much less

85   significant than those secondarily from photochemical reactions (Lv et al., 2019). Fu et

86   al. (2008) estimated that primary emissions only accounted for about 4% and 17% to

87   the total emissions of Mgly and Gly, respectively. On a global scale, isoprene and

88   ethyne are the most important precursors of Gly and Mgly; on the local scale, however,

89   degradation of aromatics is the major pathway for the production of Gly and Mgly in

90   urban and sub-urban areas. For example, the oxidation of aromatics contributed to

91   approximately 75% of Gly formation in Mexico City (Li et al., 2014; Volkamer et al.,

92   2007).

93   As for the atmospheric sink for Gly and Mgly, photolysis, reaction with OH, dry

94   deposition, and heterogenous processes are considered as the main loss pathways,

95   among which aerosol uptake is most complicated and needs more comprehensive

96   exploration (De Haan et al., 2018; McNeill, 2015; Knote et al., 2014; Fu et al., 2008).

97   The uptake of Gly and Mgly onto inorganic or organic particles has been studied in

98   laboratory experiments under controlled conditions (De Haan et al., 2018; Liggio et al.,

99   2005), and uptake coefficients (γ) were measured by the loss of gas phase concentration

or the increase of particle organic mass, within the range of $\sim 10^{-4}$ to 10^{-2} (De Haan et al., 2018; Pye et al., 2017; Liggio et al., 2005). The lower γ value was probably related to the kinetic limitations (Ervens and Volkman 2010), while the higher γ value may be associated with the increased particle acidity (Liggio et al., 2005), relative humidity (De Haan et al., 2018; Corrigan et al., 2008) and ionic strength (Kroll et al., 2005). In addition, ammonium-catalyzed and OH reactions were found to have significant influences on the surface uptake of dicarbonyls (Knote et al., 2014; Kampf et al., 2013; Noziere et al., 2008), and the rate coefficients were found to increase with the increasing ammonium ion activity (a_{NH4+}) and pH (Noziere et al., 2008). The "salting-in" effects resulted from the increased ionic strength could cause significant increase ($\sim$ 3 orders of magnitude) of henry's law constant for Gly, affecting the gas-aqueous partitioning of Gly and enhanced the available Gly for aqueous reactions (Kampf et al., 2013; Knote et al., 2014; Waxman et al., 2015).

The uptake processes of Gly and Mgly derived from the laboratory studies were incorporated into different models to investigate their formation and destruction (Ge et al., 2011; Knote et al., 2014; Pye et al., 2017). It was found that solely incorporating the irreversible uptake pathways of dicarbonyls could lead to high discrepancy between the observation and simulation results from the global 3D model and other models (Hu et al ., 2017; Li X et al., 2014; Li et al., 2013a), highlighting the needs to consider more comprehensive processes including both reversible and irreversible pathways for better simulating the dicarbonyls. Those previous studies showed that the contribution of heterogeneous processes to the destruction of dicarbonyls varied in the range of 0~80%, which depended on the relative humidity, the precursors incorporated into the model as well as the aerosol concentrations for the given region (Knote et al., 2014).

The Pearl River Delta (PRD) region has been experiencing rapid industrialization and urbanization in the last three decades, making it one of the most developed regions in China. The filed measurement results suggested that OA contributed 30~40% to $PM_{2.5}$ mass, and SOA dominated the OA with fractions up to ~80% in PRD (Huang et al., 2014; He et al., 2011). Furthermore, the contribution of SOA in $PM_{2.5}$ has been increasing in recent years, highlighting the necessity for better understanding the formation of SOA in this region (Wu et al., 2019; Wang et al., 2019). However, model simulation which provides robust information of the influence of physical processes

4

132 and chemical degradation in SOA formation still underpredict the SOA abundance with

133 only traditional VOC precursors incorporated, hindering the better understanding the

134 sources and formation mechanism of SOA in PRD (Wu et al., 2019; Fu et al., 2012;

135 Wang et al., 2009). It was found that incorporating emissions of Gly and Mgly, and their

136 degradation mechanisms could effectively narrow the gap between the measured and

137 modelled SOA (Fu et al., 2012; Li et al., 2013a). However, only the simple

138 parameterization of surface uptake of Gly and Mgly without detailed physical and

139 chemical processes (e.g., reversible partitioning of Gly and Mgly into deliquesced

140 droplets) in the model could bias the evolution of Gly and Mgly, leading to the poor

141 understanding on the budgets of Gly and Mgly, their relationship with precursors, and

142 the contributions of precursors to SOA formation in PRD (De Haan et al., 2018;

143 Waxman et al., 2015; Knote et al., 2014; Li et al., 2013a, 2014; Lu et al., 2013).

144 Therefore, to improve the model performance for the simulation of Gly and Mgly and

145 to investigate their evolution and contribution to SOA formation, the observation data

146 from a receptor site in the PRD region was analyzed by a photochemical box model

147 with near-explicit chemical mechanisms (*i.e.,* the master chemical mechanism, MCM),

148 and improvements with reversible and irreversible heterogeneous processes of Gly and

149 Mgly, and the gas-particle partitioning of oxidation products in the present study. The

150 production and evolution of Gly, Mgly, and other intermediate products were

151 investigated. The observed and simulated levels of Gly and Mgly were compared to

152 evaluate the performance of the model, which was further used to quantify the

153 contributions of individual VOCs to SOA formation at the receptor site of PRD.

154

155 **2. Methodology**

156 *2.1. Field measurement*

157 Field measurements were carried out at Guangdong provincial atmospheric

158 supersite located at Heshan (22.728°N, 112.929°E, 60 m above sea level) in Jiangmen

159 City of the PRD region. The sampling site is located about 50 km and 80 km southwest

160 from Foshan and Guangzhou City, respectively. The Heshan site is surrounded by

161 mountain areas with trees and subtropical plants, and the location of the site is showed

162 in Figure 1. Ambient measurement of VOCs, carbonyls and other trace gases was

163 conducted during January 02- 08, 2017, when the dominant wind was mainly from the

164 southeast where the center of PRD (*i.e.,* Zhuhai and Zhongshan) was located. A detailed

165 description of the Heshan site and the measurement methodology was provided in our

166 previous studies (Chang et al., 2019; Yun et al., 2018).

167
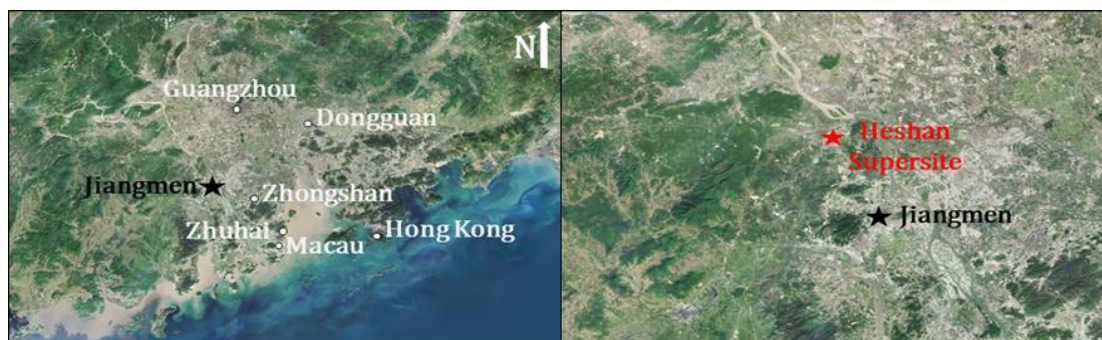
168

169 Figure. 1 The location of sampling site and its surrounding environment in the Pearl River Delta
170 region. The base map was from © Google Maps.

171

172 Briefly, mono-carbonyls, Gly and Mgly were collected with 2,4-

173 dinitrophenylhydrazine cartridges every 3 h and detected using a high-performance

174 liquid chromatography (HPLC) system (PerkinElmer 200 Series, US). The hourly

175 VOCs were measured using a cryogen-free automatic gas chromatograph system

176 equipped with a mass spectrometer and a flame ionization detector (GC-MS/FID)

177 (Wang et al., 2014). CO, SO_2, and O_3 was measured using a gas filter correlation

178 analyzer, a pulsed fluorescence analyzer, and a UV photometric analyzer, respectively

179 (Thermo Scientific 48i, 43i, 49i). NO and NO_2 were detected using a

180 chemiluminescence instrument (Thermo Scientific 42i) with a photolytic converter (Xu

181 et al., 2013). The method detection limits for non-methane hydrocarbons (NMHCs),

182 carbonyls, CO, SO_2, O_3, NO, and NO_2 were 20-300, 20-450, 4000, 100, 500, 60, and

183 300 pptv, respectively (Yun et al., 2018; Chang et al., 2019; Li et al., 2020). The

184 measurement method uncertainty of the retrieved Gly and Mgly mixing ratios was

185 estimated around 15% (Chang et al., 2019; Li et al., 2020). Furthermore, hourly

186 meteorological parameters including temperature, wind speed, wind direction, pressure,

187 and relative humidity were recorded using a pyranometer (CMP22, Kipp & Zonen B.V.,

188 Holland) and a portable weather station (Model WXT520, Vaisala, Finland).

189

190 ***2.2. Photochemical box model with master chemical mechanism (PBM-MCM) and***

191 ***gas-particle partitioning SOA scheme***

192 Photochemical box model (PBM) was employed in this study to simulate the

193 oxidation of Gly, Mgly and different VOCs, based on a master chemical mechanism

194 (MCM) coupled with a gas-particle partitioning module to represent the SOA formation

195 scheme. The MCM (version 3.2) is a near-explicit mechanism including ~16,500

196 reactions involving ~6,000 chemical species with the latest IUPAC inorganic

197 nomenclature, which described the chemical degradation of ~143 primary VOCs and

198 their oxidation products. The MCM scheme has been applied to different photochemical

199 box models to investigate the oxidation and reactivates of various VOCs, the formation

200 of photochemical O_3 and secondary organic products, atmospheric radical budget and

201 propagation, as well as the policy evaluation on mitigating the photochemical smog

202 (*e.g.,* Ling et al., 2014, 2019; Wang et al., 2017; Lyu et al., 2015; Xue et al., 2014a, b).

203 The physical processes including dry deposition and atmospheric dilution due to the

204 variations of planetary boundary layer heights (configured according to the local

205 observation in the PRD region from previous studies (Li et al., 2014; Wang et al., 2013;

206 Fan et al., 2011) were considered in the model. Similar to other box models in

207 simulating the degradation of VOCs and formation of SOA (Aumont, et al., 2012; Lee-

208 Taylor, et al., 2011; Zhang and Seinfeld, 2013), the PBM-MCM model was developed

209 by assuming a well-mixed box without consideration of vertical and horizontal

210 transport, and air pollutants were assumed to be homogeneous (Lam et al., 2013; Ling

211 et al., 2014). Thus, the influence of horizontal and vertical transport on air pollutants

212 was not considered in this study.

213 In addition to the gas-phase degradation of VOCs, a gas-particle partitioning

214 module for the oxidation products of VOCs and those compounds with an estimated

215 normal boiling temperature greater than 450 K, as developed by Johnson et al (2006),

216 were incorporated into the model to represent the SOA formation scheme (Johnson et

217 al., 2005, 2006; Kamens et al., 1999; Stein et al., 1994). In brief, the gas-to-particle

218 equilibrium partitioning of the species was described by the partitioning coefficient (K_p,

219 unit: $m^3 \mu g^{-1}$) using Eq. 1 (Johnson et al., 2006).

$$K_p = \frac{7.501 \times 10^{-9} RT}{MW_{Om} \xi P_L^0}$$ (Eq.1)

where R, T, MW_{om}, and ξ are the ideal gas constant (8.314 J K^{-1}mol^{-1}), temperature (K), the mean molecular weight of the absorbing particle organic matter (g mol^{-1}), and the activity coefficient of species in the condensed organic-phase, respectively. P^o_L is the liquid vapor pressure and was estimated using a semi-empirical expression of the Clausius-Clapeyron equation (Eq. 2):

$$\ln(\tfrac{P_L^0}{760}) = -\frac{\Delta S_{vap}(T_b)}{R}[1.8(\tfrac{T_b}{T}-1)-0.8(\ln(\tfrac{T_b}{T}))]$$ (Eq.2)

where T_b was the boiling temperature of different species, which was estimated using a previously described fragmentation method (Stein et al., 1994; Johnson et al., 2006). ΔS_{vap} (T$_b$) was the vaporization entropy change at T$_b$, which was estimated using the Trouton-Hildebrand-Everett rule with corrections for polar compounds and compounds with hydrogen-bonding capacity (Baum 1997). The concentration of species j in the condensed organic-phase ($F_{j,om}$) can be calculated as the following equation (Eq. 3):

$$F_{j,om} = M_{om} \times (K_{p,j} \times A_j)$$ (Eq.3)

where M_{om} is the total mass concentration of each condensed organic material from gas-particle partitioning, A_j is its gas-phase concentration, and $K_{p,j}$ is its partitioning coefficient of species j (Johnson et al., 2006).

The partitioning process was dynamically represented as an equilibrium between absorption and desorption, as described by Kamens et al. (1999). Briefly, the species-dependent K_p values were defined in terms of absorption (k_{in}) and desorption (k_{out}) rate coefficients, with $K_p = k_{in}/k_{out}$. The value for k_{in} ($k_{in} = 6.2 \times 10^{-3}$ m^3·µg^{-1}·s^{-1}) was configured as suggested by Johnson et al. (2006). Thus, the K_p could be expressed in terms of k_{out}. More detailed description of the equations and parameters are given by Johnson et al. (2005, 2006) and Kamens et al. (1999).

The above gas-particle partitioning of low volatility compounds formed by the gas-phase oxidation of VOCs and other precursors (Aumont, et al., 2012; Lee-Taylor et al., 2011) was configured in the model to estimate the SOA formation. However, the recent experimental results suggested that the formation of SOA in laboratory chambers may be suppressed due to losses of SOA to chamber walls, which leads to

8

249 underestimates of SOA in air-quality and climate models (Matsunaga and Ziemann

250 2010; Zhang et al., 2014). Therefore, to consider the wall loss of SOA, the average wall

251 loss rate coefficient of 6×10^{-5} s^{-1} was adopted in the model configuration according to

252 previous studies on the basis of calculated organic material using an assumed density

253 of $1 g \cdot cm^{-3}$ (Johnson et al., 2004, 2005). In addition, the wall loss of other gaseous

254 compounds (O_3, NO_2 and HNO_3) were implemented in the box model with the average

255 parameters of 3×10^{-6} s^{-1}, 1.15×10^{-5} s^{-1} and 8.2×10^{-5} s^{-1}, respectively. The detailed

256 information for the calculation of above parameters was provided in Bloss et al. (2015).

257

258 ### *2.3. Partitioning and reactions of gas-phase dicabonyls on particles*

259 The partitioning and reactions of dicarbonyls in the aerosol aqueous phase may

260 involve both irreversible and reversible processes (Ervens and Volkamer, 2010). In the

261 present study, we follow the mechanism proposed by Knote et al. (2014) and consider

262 the reversible partitioning in aqueous phase, the irreversible volume reactions and

263 irreversible surface uptake processes in our model.

264 The reversible partitioning of Gly and Mgly on aerosols aqueous phase is usually

265 described by the Henry's law equilibrium (Kampf et al., 2013) (Eq.4):

266 $[Gly(Mgly)]_{liquid} = K_H \times [Gly(Mgly)]_{gas}$ (Eq.4)

267 However, hydration of carbonyls function groups and salt-Gly interactions could have

268 significant influences on the K_H value of Gly (Kampf et al., 2013; Waxman et al., 2015),

269 and an effective Henry's law coefficient expressed by Eq.5 was often used.

270 $$K_{H,effective} = \frac{K_{H,water}}{10^{(-0.24\min(12.0,(C_{as}+C_{an}))}}$$ (Eq.5)

271 where the C_{as} and C_{an} represent the concentrations of ammonium sulfate and nitrate.

272 The detailed information on each parameter in these equations have been provided in

273 Kampf et al. (2013), Waxman et al. (2015) and the supplementary of the present study.

274 As variations were found for the value of $K_{H,effective}$ under different concentrations of

275 ammonium sulfate and nitrate in previous studies (Knote et al., 2014; Kampf et al.,

276 2013; Erverns and Volkamer, 2010), the C_{as} and C_{an} were calculated every hour in the

present study from the measured ammonium sulfate (and ammonium nitrate) concentrations (mol m^{-3}) divided by aerosol liquid water content (ALWC, kg m^{-3}), which were determined by the aerosol inorganics model (AIM-IV, http://www.aim.env.uea.ac.uk/aim/model4/model4a.php) with inputs of the observed parameters (*e.g.*, ambient relative humidity, temperature, and the moles of each ion) at the Heshan site (Chang et al., 2019).

The reversible formation of monomer (*i.e.*, glyoxal, glyoxal monohydrate, and glyoxal dihydrate) and oligomers are considered with the two important reservoirs (*i.e.,* monomer and oligomer pools, represented as pool1 and pool2) (Knote et al. 2014). The variations of the glyoxal monomer ([Gly$_{p1}$]) and oligomer concentrations ([Gly$_{p2}$]) with time can be represented by the following equations (Erverns and Volkamer, 2010; Kampf et al., 2013; Knote et al., 2014):

$$\frac{d([Gly_{p1}])}{dt} = \frac{1}{\tau_1} \times (Gly_{p1,eq} - Gly_{p1}) \,(Eq.6)$$

$$\frac{d([Gly_{p2}])}{dt} = \frac{1}{\tau_2} \times (Gly_{p2,eq} - Gly_{p2}) \,(Eq.7)$$

$$\frac{Gly_{p2,eq}}{Gly_{p1,eq}} = K_{olig} \quad (Eq.8)$$

The equilibrium partitioning between monomers and oligomers was presented as K_{olig} (Eq.8). The definition and configuration of each parameters above were provided in the supplementary (Section S2) according to Knote et al. (2014) and Kampf et al. (2013).

In addition, three irreversible pathways of Gly, including 1) the ammonium-catalyzed volume pathway, 2) the OH-reaction volume pathway, and 3) the irreversible surface uptake, were parameterized in the model (Knote et al., 2014; Ervens and Volkman 2010). The ammonium-catalyzed reactions, with rate constant depending on both particle acidity (pH) and the activity of the ammonium ion (a_{NH4+}), were parameterized as follows when the monomer and oligomer concentrations were in equilibrium (Eq. 9):

$$K = 2 \times 10^{-10} \times \exp(1.5 \times a_{NH_4}) \times \exp(2.5 \times pH) \times Gly_{p1} \quad (Eq.9)$$

303   This parameterization was configured based on the assumption that only total

304 concentration in the monomer pool was the only particulate glyoxal available to the

305 ammonium-catalyzed reaction as the reversibly formed oligomers do not evaporate

306 easily (Knote et al., 2014; De Haan et al., 2009; Noziere et al., 2008).

307   For OH pathway, the gas-phase OH was in equilibrium with liquid-phase OH by

308 a Henry's law constant ($K_{I,OH}$= 25 M atm^{-1}) with the consideration of the "salting-in"

309 impact (Ervens and Volkamer 2010), and constant of reactions between OH and Gly

310 was 1.1×10^{-9} M^{-1} s^{-1} (Buxton et al., 1997). As suggested by Knote et al. (2014), the Gly

311 concentration available to the OH-reaction pathway was the total glyoxal concentration

312 in the monomer pool.

313   Surface-controlled irreversible uptake of Gly has been widely employed in

314 different modeling studies (Ervens et al., 2011; Li et al., 2014; Liu et al., 2007), was

315 parameterized as follows (Eq.10):

316
$$K_r = -\frac{\gamma_{gly(mgly)} \times S_{aw} \times v_{gly(mgly)} \times C^{*}_{gly(mgly)}}{4} \quad \text{(Eq.10)}$$

317   where C^{*} and v are the gas-phase concentration and mean molecular velocity,

318 respectively. γ represents the uptake coefficient for Gly and Mgly. Here we use the

319 surface uptake coefficients (γ_{gly}= 1.0×10^{-3} and γ_{Mgly}= 2.6×10^{-4}) to account for the

320 irreversible surface uptake of Gly and Mgly, respectively. It is noted that the surface

321 uptake coefficient of Gly was configured according to the results of uptake kinetics

322 experiments from Schweitzer et al. (1998), which has been used in the model simulation

323 of Gly in the previous PRD study (Li et al., 2014). On the other hand, the surface uptake

324 coefficient of Mgly was obtained via scaling to glyoxal uptake coefficient by the

325 relative Henry's low coefficient suggested by Pye et al. (2017). S_{aw}

326 (S_{aw}=S_a×f(RH)=S_a×(1+a×(RH)^b)) is the RH corrected aerosol surface area density (Li

327 et al., 2014). The value for a (2.06) was configured as those suggested previously (Liu

328 et al., 2007), while the dry aerosol surface concentration (S_a) was obtained from the

329 measurement at the Heshan site (Yun et al., 2018). In this study, the mean molecular

330 velocities of Gly were calculated by the HyperPhysics model (http://hyperphysics.phy-

astr.gsu.edu/hbase, last access date: 06 June 2019). The carbonaceous and insoluble components were considered as an aqueous shell for aerosols, whereas the aerosol surface was fully covered with an aqueous layer (Li et al., 2015).

On the other hand, though heterogeneous processes of Mgly are similar to those of Gly, some difference between these two species were found. The Henry's law constant for Mgly is not as effective as that for Gly. Hence, a Henry's law constant (3.7×10^3 M atm^{-1}) for Mgly we used (Zhou and Mopper 1990). In fact, Kroll et al. (2005) suggested that no obviously aerosol growth was observed from gas-phase Mgly presumably because of its more stable (less electron deficient) ketone moiety, and a recent study indicated that less Mgly would partition into the aerosols than expected according to Henry's law (Waxman et al., 2015). In addition, the surface uptake coefficient ($\gamma_{Mgly} = 2.6 \times 10^{-4}$) suggested by Pye et al. (2017) is lower than that extracted from the chamber study (De Haan et al., 2018), which reported the value of γ_{Mgly} could increase to 3.7×10^{-3} at 95% RH and even larger than Gly in a high relative-humidity environment ($\geq 95\%$). However, they also figured out that treating the surface uptake of Mgly on aerosols as an irreversible pathway could probably overestimate its positive effect for SOA formation via heterogeneous processes, because ~20% of SOA which were formed from Mgly via aqueous processes would further hydrolyze.

2.4. Model scenarios

According to the discussion above, it could be seen that the heterogeneous processes we described for Gly was more complicated than that for Mgly, as the parameterization for the sink of Gly from laboratory and model studies were more robust. Therefore, the present study put more emphasis on the evolution of Gly for better understanding and evaluating the effects of the different sink pathways on dicarbonyls and its influence on SOA formation. Table 1 provides detailed information regarding all the model scenarios for the simulation of Gly, while the model scenarios for Mgly are also given in Table S1 in the supplementary.

Table 1. Model scenarios used for gas-phase Gly

Scenarios	Description	Purpose
INITIAL	Default MCMv3.2, without considering the reversible and irreversible uptake of Gly and the gas-particle partitioning of other oxidation products	Base run
scenario 1	As INITIAL, also considers ammonium-catalyzed reactions of Gly through monomers pool 1 without the reversible formation of oligomers pool 2.	Investigating the influence of Ammonium reactions on the destruction of Gly
scenario 2	As scenario 1, also considers OH reactions of Gly through monomers pool 1 without the reversible formation of oligomers pool 2.	Investigating the influence of OH reactions for the destruction of Gly
scenario 3	As scenario 2, and considers the aqueous oligomers formation (pool 2) and revisable process with monomers (pool 1).	Investigating the "salting in" impact
scenario 4	As scenario 3, and considers surface uptake by aerosols of Gly with the uptake coefficient of 1×10^{-3} suggested by Li et al. (2014).	Investigating the influence of surface uptake

360

In this study, hourly observation data of CO, SO_2, NO, NO_2, O_3, NMHC and meteorological parameters were used as input and constraints in the model. By taking the NMHC species incorporating in the MCM mechanism into account (MCM website, http://mcm.leeds.ac.uk/MCM/roots.htt, access date: 22 June 2020), observations of total 44 NMHC species, including 18 alkanes, 11 alkenes, ethyne and 14 aromatics were used as input for the model simulation (Table S2 in the supplementary). The selected NMHCs contributed about 98% and 99% to the total mixing ratios and photochemical reactivities of all measured NMHCs at the Heshan site. Furthermore, the selected VOCs are the major precursors for Gly, Mgly, photochemical O_3 and SOA (Ding et al., 2016, 2017; Li et al., 2014; Lou et al., 2010; Yuan et al., 2013), and have been frequently used to drive box model for studies on SOA, photochemical O_3 and photochemical reactivity (Hofzumahaus et al., 2009; Lee-Taylor, et al., 2011).

The photolysis rates, which were not measured, were modified in the model using the photon fluxes from the Tropospheric Ultraviolet and Visible Radiation (TUV-v5) model (Madronich and Flocke 1997) according to the sampling location and modeling period. Model simulation on Gly and Mgly was performed on January 07-08, 2017, when both daily Gly and Mgly data were available, with 00:00 LT (local time) as the

378   initial time. Before the simulation, the model was pre-run for 5 days using the observed
379   variability of the input species during the whole sampling period to achieve a steady
380   state for the unmeasured species with a short lifetime, *i.e.,* OH and HO_2 radicals (Xue
381   et al., 2014a, b).

382   In this study, the simulation on the diurnal variations of OH and HO_2 was
383   performed well, with peak values at noon, consistent with those measured and
384   simulated in PRD (Hofzumahaus et al., 2009 and related papers; Tan et al., 2019). The
385   simulated mean mixing ratios of OH and HO_2 radicals from the model in the present
386   study were $\sim 1.6 \times 10^6$ molecule·cm^{-3} and $\sim 3 \times 10^7$ molecule·cm^{-3}, which are comparable
387   to the winter observations at Beijing, Tokyo, and New York (Kanaya et al., 2007; Ren
388   et al., 2006; Ma et al., 2019), and lower than the measurement and simulation values in
389   summer (e.g., July) or autumn (e.g., October to November) in the PRD region (Table
390   S3 in the supplementary) (Hofzumahaus et al., 2009; Tan et al., 2019). Note that the
391   variations of simulation results in the present study and those observation results in
392   previous studies in PRD may be associated with differences in the levels of O_3 and its
393   precursors, different photolysis rates, and to a lesser extent, meteorological conditions
394   (Hofzumahaus et al., 2009). The higher OH and HO_2 mixing ratios were expected in
395   summer and autumn than winter due to the stronger solar radiation and higher
396   temperature, as well as the variations of O_3 and its precursors in different sites, though
397   the measurement of OH/HO_2 radicals has been very challenging, and significant
398   uncertainties still exist in the measurement values of the radicals (Hofzumahaus et al.,
399   2009; Tan et al., 2019). Furthermore, the comparison between the simulation of a box
400   model and observation results suggested that the higher observed mixing ratios of OH
401   and HO_2 radicals were related to an unidentified source of OH at the backgarden site of
402   PRD in summer of 2006, while the comparison between the observed OH/HO_2
403   variations and those calculated from the parameterization of HO_x (HO_x = OH + HO_2)
404   production and destruction indicated a missing OH source of 4-6 ppbv·h^{-1} and an
405   unknown RO_2 loss at the Heshan site in autumn of 2014.

406   In addition to the simulation of OH and HO_2 radicals, as there were no direct
407   measured SOA data in this study (Chang et al., 2019), the model performance was

408   evaluated by the comparison between the model simulated SOA with those calculated

409   using the EC (elemental carbon)-tracer method, and by the comparison between the

410   simulated and observed concentrations of other secondary products, which have been

411   provided in detail in the supplementary (Section S3). For example, the simulated

412   concentration of SOA was about 85% of those calculated by the EC-tracer method

413   based on the observed hourly data (Chang et al., 2019). Furthermore, the simulated

414   concentrations of acetic acid, formic acid and pyruvic acid were close to those observed

415   at the Heshan site, accounting for ~80%, 70% and 88% of observed values for acetic

416   acid, formic acid and pyruvic acid, respectively. The results confirmed that secondary

417   formation was the dominant source of above species at the Heshan site, and suggested

418   that the PBM-MCM model could provide robust performance on simulating the

419   abundance of above secondary species and SOA.

420

421   ### *2.5. Model uncertainty*

422   Uncertainties in the simulation of Gly and Mgly by the model were noted. The total

423   model errors could be calculated conservatively from 1) the uncertainties in the

424   measurement of trace gases and NMHCs; 2) the measured data of meteorological

425   parameters, *i.e.,* temperature T, pressure P, and the calculated photolysis frequencies J

426   based on meteorological conditions; 3) reaction rate constants k; and 4) the dry

427   deposition. In this study, following Li et al. (2014) and Lu et al. (2013), the uncertainty

428   factors for the above parameters were adopted as suggested previously (Table S4 in the

429   supplementary), and all parameters were divided into three groups (*i.e.,* physical

430   parameters, radical and trace gas concentrations, and reaction rate constants of non-

431   photolytic reactions). Each parameter was multiplied by its uncertainty factor first, and

432   the gaussian error propagation was then applied within each group. We run the model

433   n times (n is the number of parameters considered). The mean diurnal variation of the

434   uncertainty of modeled Gly and Mgly is shown in Figure S1. The total uncertainties of

435   the modelled Gly and Mgly were both estimated to be around 39% with the

436   contributions from radical and trace gas concentrations (~19%), physical parameters

437   (~13%) (included photolysis frequencies, deposition lifetime, T, etc.) and reaction rate

438   constants of non-photolytic reactions (~7%), respectively.

439

3. Results and Discussion

#### 3.1. Comparison between the simulation and observation

In this study, the simulated Gly and Mgly were secondarily formed from the oxidation of their VOC precursors. Therefore, before the comparison between the simulation and observation results, the contributions of primary and secondary sources to the measured Gly and Mgly were preliminarily estimated by a correlation-based source apportionment method suggested by previous studies (Friedfeld et al., 2002; Yuan et al., 2013). Table S5 in the supplementary shows linear regression coefficients and relative source contributions of Gly and Mgly. It was found that the contributions from primary sources (3.46% and 3.51% for Gly and Mgly, respectively) were significantly lower than those from secondary sources (96.14% and 96.44%, respectively), confirming that observed Gly and Mgly in the present study were mostly related to secondary formation.

The simulated Gly and Mgly from the photochemical box model under different scenarios were examined and compared with the observation. The predicted Gly and Mgly from in-situ formation in the INITIAL scenario was found to generally overpredict the mixing ratios of Gly and Mgly, and were about 3.3 and 3.5 times of the observed concentrations at the Heshan site, respectively. Similar overestimation has been reported in previous modeling studies, for example, the simulations with only the MCM gas-phases schemes overpredicted the Gly concentration by factors of 2-6 in both urban Mexico City (Volkamer et al., 2007) and a semi-rural site of the PRD region (Li et al., 2014). The significant overestimation in simulation results indicated that there were important loss pathways for Gly and Mgly other than the oxidation reactions (*e.g.,* by OH and NO_3 radicals). A sensitivity analysis was firstly conducted with twice the dilution rate (and deposition velocities) in INITIAL scenario, which resulted in the reduction of modeled concentrations of Gly and Mgly by 9.2% (3.2%) and 7.9% (2.8%), respectively (Table S6 in the supplementary). Though these enlarged rates were higher than the upper limits of the dilution rate and deposition velocities in previous studies (Fan et al., 2011; Wang et al., 2013; Li et al., 2014), the predicted mixing ratios of Gly and Mgly were still three times higher than the measured levels, suggesting that the

16

470 dilution and dry deposition configuration could not be the main causes for the

471 overestimation of modeled Gly and Mgly mixing ratios (Volkamer et al., 2006, 2007).
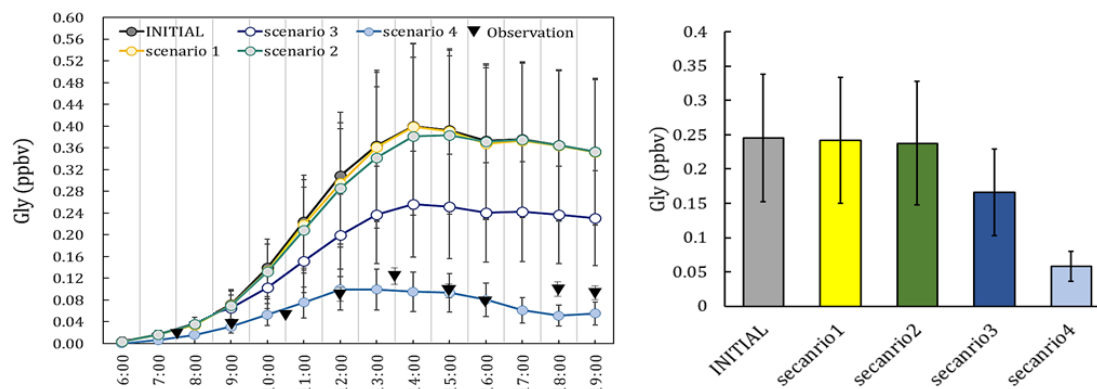
472

473 Figure 2. The observation data, the concentrations and the daily average concentration of Gly
474 predicted from the different scenarios.

475

476   To identify the causes of discrepancy and improve model performance, sensitivity

477 analysis with different heterogenous mechanisms incorporated in the model scheme (as

478 scenarios listed in Table 1) was conducted. The average diurnal patterns of Gly

479 simulated by different model scenarios are showed in Figure 2. It can be seen that in

480 the early morning (*i.e.*, 0600 to 0800 LT, local time), the predicted mixing ratios of Gly

481 in different scenarios were comparable to the observation. In contrast, the difference

482 became larger from 0900 LT onwards, though the predicted peaks of Gly by different

483 model scenarios were all presented at the early afternoon, following by a slow decrease

484 in the late afternoon. The model results from Scenario 4 was more consistent with the

485 observational data. The relative changes of modeled Gly concentrations by adding

486 additional heterogeneous processes to the model scenario INITIAL (*i.e.*, model

487 scenarios 1-4) were summarized in Table S7 in the supplementary.

488   On average, by including additional irreversible and reversible pathways, the

489 modeled Gly concentrations during daytime (06:00-19:00) decrease by 72.3% of the

490 values predicted by the INITIAL scenario, and a significant decrease of Gly

491 concentration occurred by adding the effect of surface uptake pathway (*i.e.*, model

492 scenarios 3-4). Similar results have been obtained in a previous study in summer in the

493 PRD region (Li et al., 2014), which found that the simulated Gly concentration decrease

494 significantly (~45 %) in the daytime (*i.e.*, 0600 to 1900 LT) when heterogeneous uptake

495 process was considered with the incorporation of a single uptake coefficient.

496   The contribution of different heterogeneous sink pathways is calculated based on

the scenario 4 (Figure S2). The irreversible pathways of Gly (*i.e.*, surface uptake by aerosols, OH and ammonium reactions) accounted for 67.3% of the total sink of Gly, among which the surface uptake was a dominant pathway (62%) comparing to the ammonium and OH reactions (2.4% and 2.9%, respectively). The reversible pathway made a relatively lower contribution to the total sink of Gly (32.7%).

In addition, the heterogeneous irreversibly and reversibly pathways of Mgly was also investigated in the sensitivity analysis (*i.e.*, model scenarios M1-2, listed in Table S8 in the supplementary), and the predicted Mgly concentrations during daytime (0600-1900 LT) decreased by 73.0% of the values estimated in INITIAL model scenario. The surface uptake pathway in the scenario M2 was found to be the most important heterogeneous pathway for the loss of Mgly, and contributed to 64.1% of the total heterogeneous sink of Mgly. The contributions of the reversible pathway to the destruction of Mgly was around 35.9% (Figure S3).

Overall, by incorporating a more detailed heterogeneous processes of Gly and Mgly, the results of scenarios 4 and M2 provided better agreement between the modeled and measured Gly and Mgly. The results demonstrated the significance of heterogeneous uptake processes on the destruction of Gly and Mgly, and adopting the irreversible/reversible pathways (*i.e.*, the reversible partitioning, volume reactions, and the surface uptake) could reasonably reproduce the variations of Gly and Mgly at the Heshan site in the PRD region.

3.2. Process analysis on the production and destruction of Gly and Mgly

The scenarios 4 and M2 simulation with the best agreement with measurement were further analyzed to investigate the photochemical budget of Gly and Mgly at the Heshan site, respectively (Table 2 and Table S1). It was found that OH oxidation of aromatics was the most important contributor for the Gly and Mgly production, with mean contributions of ~80% and ~94%, respectively. Among all the aromatic precursors, toluene and *m,p*-xylene were the two major precursors for the formation of Gly and Mgly, with total contributions of ~43% and ~56% of Gly and Mgly formation, respectively. In contrast, because of the relatively low photochemical reactivity, benzene and alkanes had lower contributions to the formation of Gly and Mgly, although they can travel a long distance and contribute to secondary Gly and Mgly in

529   areas far from their emissions (Lv et al., 2019). Different from previous studies that

530   found the isoprene as the key precursor for Gly and Mgly formation (Li et al., 2014;

531   Lou et al., 2010), the contributions of isoprene oxidation at the Heshan site in the

532   present study were much lower than that of aromatics, with only mean contributions of

533   ~2% and ~3%, respectively. It can be attributed to the lower mixing ratios of isoprene

534   (*i.e.,* 70 ± 10 pptv) observed at the Heshan site because of the lower temperature in

535   winter, comparing to the much higher concentration observed during summer (average

536   of ~1 ppbv and maximum of ~ 4 ppbv in the afternoon) in the rural and forest areas in

537   this region (Li et al., 2014; Lou et al., 2010).

538   In addition, the relative contributions of different loss pathways of Gly and Mgly,

539   including physical processes (vertical dilution and dry deposition), reaction with

540   radicals (e.g., OH and NO_3), and the heterogeneous processes of Gly and Mgly on

541   aerosols at daytime were also estimated from the PBM-MCM model results (Table 2).

542   Consistent with previous studies (Atkinson and Arey, 2003; Ervens et al., 2011),

543   heterogeneous processes were the most important pathway for the destruction of Gly

544   and Mgly (with contributions of ~62% during daytime), followed by photolysis (with

545   contributions of ~26% and ~25%, respectively). It should be noted that the oxidation

546   of Gly and Mgly by O_3 was not considered in this study as the reaction rate constants

547   of Gly and Mgly with O_3 are < 3 and < 6 × 10^{-21} $cm^3 \cdot molecule^{-1} \cdot s^{-1}$, respectively,

548   which are 6 order of magnitude lower than the reaction rate constants with NO_3

549   (which >1 and > 2 × 10^{-15} $cm^3 \cdot molecule^{-1} \cdot s^{-1}$, respectively), and are 9 order of

550   magnitude lower than the reaction rate constants with OH (9 and 13 × 10^{-12}

551    $cm^3 \cdot molecule^{-1} \cdot s^{-1}$ for the reactions of Gly and Mgly with O_3, respectively) (Mellouki

552   et al., 2015). Therefore, we believe that the influence of O_3 on the removal of Gly and

553   Mgly was negligible (Mellouki et al., 2015). Furthermore, there were few

554   parameterizations for the reaction mechanism of Gly/Mgly with O_3 due to their low

555   reaction rates with O_3.

556   On the other hand, at nighttime, only the heterogenous processes made the main

557 contribution to Gly and Mgly destruction, with contributions higher than 90% to the

558 total destruction of Gly and Mgly at night (Table S9 in the supplementary), consistent

559 with previous studies (Washenfelder et al., 2011; Gomez et al., 2015). The lower

560 contributions of Gly and Mgly with radicals were mainly because of the low OH

561 concentration at night and their relatively lower reactivities with NO_3 radical (e.g., the

562 reaction rate constants of Gly/Mgly with NO_3 are ~1000 times lower than those with

563 OH radical) (Calvert et al., 2011; Mellouki et al., 2015).

564

565 Table 2 Production and destruction of Gly and Mgly from model simulation at daytime

Precursor	Oxidant	Gly		Mgly	
		Molar yield (%)[a]	Contribution (%)	Molar yield (%)[a]	Contribution(%)
Aromatics					
benzene, %	OH	32	4.94	-	-
toluene, %	OH	30.6	23.41	21.5	23.80
m, p-xylene, %	OH	25.2	19.22	35.1	32.08
o-xylene, %	OH	12.7	15.04	33.1	14.49
1,2,4-trimethylbenzene, %	OH	7.2	1.40	27.2	5.98
1,2,3-trimethylbenzene, %	OH	7.8	1.43	15.1	4.54
1,3,5-trimethylbenzene, %	OH	-[c]	-	58.1	13.21
ethylbenzene, %	OH	55	6.62	-	-
p-ethyltoluene, %	OH	31.9	5.45	-	-
m-ethyltoluene, %	OH	7.9	1.52	-	-
o-ethyltoluene, %	OH	8	0.51	-	-
Sum			79.54		94.10
Alkanes					
propane, %	OH	-	-	11	0.73
> C3 alkanes[b],%	OH	1	0.19	3.2	0.71
Sum			0.19		1.44
Alkenes					
isoprene,%	OH	6.2	0.43	25	0.57
	NO_3	43.7	1.34	37.8	2.83
	O_3	4	0.20	-	-
ethene,%	OH	5.7	1.08	-	-
	O_3	0.44	1.15	-	-

20

> C2 alkenes[b],%	OH	-	-	7.7	1.06
propene, %	O_3	8.3	1.01	-	-
1-pentene, %	O_3	2	0.73	-	-
Sum			5.94		4.46
Acetylene	OH	63.5	14.33	-	-
Loss pathyways					
photolysis, %			26.2		25.1
NO_3,OH- reaction, %			4.06		7.87
dry deposition, %			2.23		1.73
dilution, %			5.71		3.30
heterogeneous [d], %					
Irreversible processes, %			41.0		39.8
Reversible processes, %			20.8		22.2

[a] Molar yields were taken from previous studies (Fu et al., 2008) (Fick et al., 2003) (Nishino et al., 2010) (Calvert 2000; Volkamer et al., 2006).

[b] >2 alkenes (include 3 alkenes) and >3 alkanes (include 17 alkanes) are represented in this study as a single lumped species (Lv et al., 2019).

[c] "–" not applicable.

[d] Considered both irreversible and reversible parameterizations of the aerosol sinks (*i.e.*, scenario 4 and M2 in the supplementary).

3.3 Implications for secondary organic aerosol formation

By incorporating both the traditional gas-particle partitioning (of VOC oxidation products) and the heterogeneous processes (of Gly and Mgly) into the model, we investigated the contributions of different mechanism in SOA formation through sensitivity analysis. The contributions of VOC oxidations to SOA formed from gas-particle partitioning (SOA_{gp}) and SOA formed from heterogeneous processes of Gly and Mgly (SOA_{het}) were quantified.

On the other hand, only based on the SOA_{gp} formation scheme, the relative importance of each VOC precursor in SOA_{gp} formation was further evaluated to provide a complete picture for SOA_{gp} formation and its relationship with precursors. As with O_3 formation, the roles of individual VOC precursors in SOA_{gp} formation were calculated using relative increment reactivity (RIR_{SOAgp}) method, which have been widely used to present the percentage change in the production of secondary products per percent change in precursors. The RIR_{SOAgp} of a specific precursor X at site Z is given by Eq. 11:

589 $$RIR_{SOA_{gp}}^{Z}(X)=\frac{[P_{SOAgp}^{Z}(X)-P_{SOAgp}^{Z}(X-\Delta X)]/P_{SOAgp}^{Z}(X)}{\Delta Z(X)/Z(X)} \quad (Eq.11)$$

590   where $Z(X)$ represents the measured concentration of precursor X, including the
591   amounts emitted at the site and those transported to the site, and ΔX is the change in the
592   concentration of precursor X caused by a hypothetical change $\Delta Z(X)$ (10% $Z(X)$ in this
593   study). Here, $P_{SOA_{gp}}^{Z}(X)$ represents the SOA$_{gp}$ formation potential. A large positive
594   RIR_{SOAgp} value of a specific precursor suggests that SOA$_{gp}$ formation could be
595   significantly decreased if the emissions of this precursor were controlled. Figure 3
596   depicts the top 10 VOC precursors with high RIR_{SOAgp} values at day time. Both m,p-
597   xylene and o-xylene had the highest RIR_{SOAgp} value (~0.35), followed by toluene (~0.2)
598   and ethylbenzene (~0.06). As m,p-xylene, o-xylene and toluene can also have a
599   significant impact on dicabonyls production, they are likely to make a noticeable
600   contribution to both SOA$_{gp}$ and SOA$_{het}$ formation.
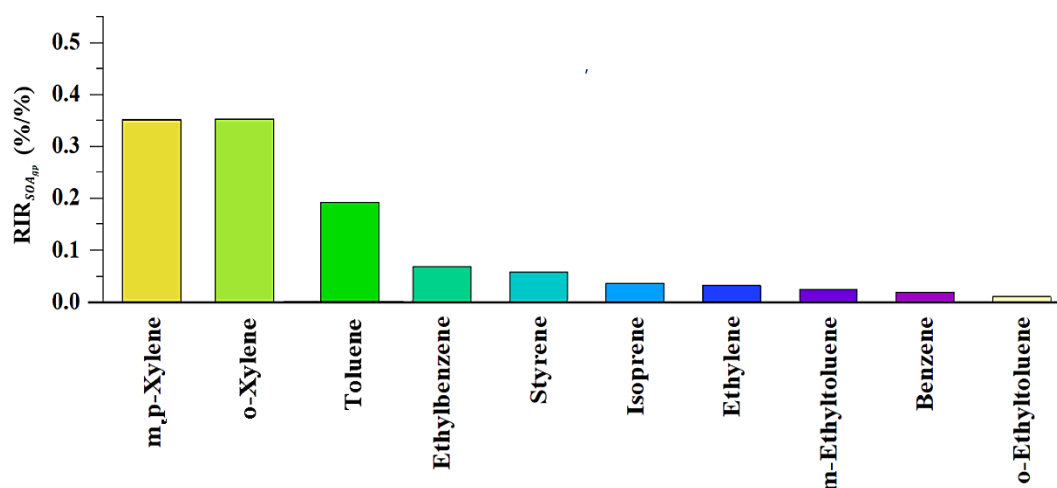
601
602   Figure 3. Top 10 VOC precursors with high RIR_{SOAgp} values at daytime.

603   The SOA production from Gly and Mgly was further explored by the model
604   simulation with and without the consideration of Gly and Mgly. It was found that by
605   incorporating the evolution of Gly and Mgly, the SOA production has been improved
606   apparently from 1.83 to 2.47 $\mu g/m^3$. The total contribution of the Gly and Mgly
607   contributed ~26% to the simulated SOA concentrations, of which ~21% was from the
608   heterogeneous processes of Gly and Mgly (SOA$_{het}$), further demonstrating that the
609   heterogeneous processes have significant influences on the SOA formation from Gly
610   and Mgly.

611   To further highlight the roles of heterogeneous processes of Gly and Mgly on the
612   SOA production (SOA$_{het}$) and to evaluate the contributions of different VOCs, the

average diurnal variations of SOA_{het} concentration formed from the heterogeneous processes of Gly and Mgly were showed in Figure 4. Both SOA_{het} (Gly) and SOA_{het} (Mgly) concentrations presented photochemistry-driven diurnal patterns, and started to increase in the morning before reaching the maximum value (0.52 and 0.42 $\mu g/m^3$) at 1400 and 1200 LT, respectively. It is consistent with the diurnal pattern of SOA_{gp}, which could be formed from the oxidation of VOCs (including NMHCs and the gaseous oxidation of Gly and Mgly which were formed from the oxidation of NMHCs), due to the high photochemical reactivity at noon, which further converted to SOA_{gp} through gas-particle partitioning. In general, SOA_{gp} made a higher contribution to total SOA (78.6%) than SOA_{het} (21.4%). Previous studies have indicated that the more abundant anthropogenic precursors than biogenic ones under NO_x saturated environment could lead to greater contribution of SOA_{gp} to total SOA despite that the oxidation of anthropogenic species (*i.e.*, aromatics) could lead to relatively higher yields of Gly and Mgly (Knote et al., 2014; Ervens et al., 2011). Ervens et al. (2011) has found that in areas with high concentrations of biogenic precursors at high relative humidity, the SOA_{het} and SOA_{gp} were equally important for total SOA, while in the anthropogenic dominated areas, the contribution of SOA_{het} to the total predicted SOA mass was around 30%. Similarly, the formation of SOA_{gp} and SOA_{het} were both dominated by xylenes and toluene, contributing to ~74%, ~62% and ~69% of SOA_{gp}, SOA_{het} (Gly) and SOA_{het} (Mgly), respectively. Furthermore, *o*-xylene was the most important precursor to the SOA_{gp} (~29%), but only contributed ~16% and ~13% to SOA_{het} (Gly) and SOA_{het} (Mgly) formation, respectively. The toluene and *m,p*-xylene made the most significant contributions to the SOA_{het} (Gly) (~26%) and SOA_{het} (Mgly) (~32%) formation, respectively, consistent with the chamber results from the oxidations of different precursors (Ervens et al., 2011).
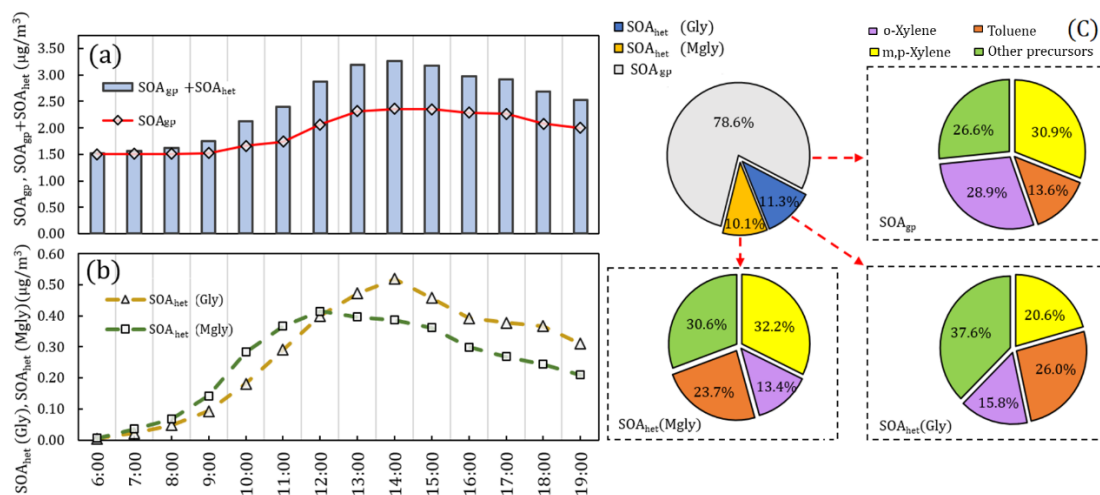
Figure 4. The average diurnal variations of SOA_{gp}, SOA_{het} (Gly) (*i.e.*, SOA_{het} formed from heterogeneous processes of Gly), SOA_{het} (Mgly) (*i.e.*, SOA_{het} formed heterogeneous processes from Mgly) and total SOA formation (SOA_{gp} + SOA_{het}) were showed in Figure 4a and 4b. The proportion of SOA_{gp}, SOA_{het} (Gly) and SOA_{het} (Mgly) in total SOA as well as the contribution of VOCs precursors to SOA_{gp}, SOA_{het} (Gly) and SOA_{het} (Mgly) formation, were represented in the pie charts in Figure 4c.

3.4 Comparison with previous studies in PRD

Previous studies have been conducted to investigate the evolution of Gly and/or Mgly using observation and model simulation in the PRD region. However, one must bear in mind that the mechanisms of the formation and evolution of Gly and/or Mgly were more detailed in the present study, as previous studies in PRD only incorporated the irreversible surface uptake process with a single coefficient for the heterogeneous pathway for dicarbonyls. This may not reflect the current knowledge for the formation and evolution of Gly and/or Mgly and their influence on SOA formation (Knote et al., 2014; Waxman et al., 2015; Sumner et al., 2014).

Li et al. (2013a) used the regional air quality model CMAQ to investigate the contributions of the aerosol surface uptake of Gly and Mgly to SOA formation in the PRD region, and an uptake coefficient of 2.9×10^{-3} was used for both Gly and Mgly in the model. Interestingly, the results from their model were about 30% higher than that in our study (Table S10 in the supplementary). For example, Li et al. (2013a) concluded that SOA formed from the heterogeneous processes of dicabonyls may contribute higher than 50% to the total SOA mass in the PRD region, while our study showed that the contribution of SOA_{het} to total SOA mass was ~21% (*i.e.*, ~11% of SOA_{het} formed from Gly; ~10% of SOA_{het} formed from Mgly). In addition, the averaged concentration of SOA_{het} from Gly (0.28 µg/m³) and Mgly (0.25 µg/m³) in our study is one order of

magnitude lower than that in Li et al. (2013a) (*i.e.*, 2.33 and 2.51 μg/m^3, respectively). The discrepancy was mainly due to the different parameterizations of heterogeneous processes of dicarbonyls. The parameterization in the Li et al. (2013a) and other previous studies did not consider the reversible processes of dicarbonyls, but used one constant surface uptake coefficient to represent all the heterogeneous processes, which could result in bias in SOA formation if there are available aerosol surfaces without considering the influence of aerosols composition and phase state. Moreover, most of the previous studies using higher surface uptake coefficients intended to narrow the discrepancy between observed and simulated SOA mass without direct comparison between observed and simulated concentrations of dicarbonyls (i.e., Li et al., 2013a; Waxman et al., 2013; Fu et al., 2008; Vokalmer et al., 2007). For example, Knote et al. (2014) conducted a total of seven simulations to investigate the SOA formation from Gly over California. Their results showed that the SOA concentration in SIMPLE scenario (characterized by a single uptake coefficient of 3.3×10^{-3}) was an order of magnitude higher than that in HYBRID scenario (characterized by an uptake coefficient of 1.0×10^{-3} and also considered more comprehensive parameterization of heterogeneous processes). In fact, if we only consider the surface uptake by aerosols for dicarbonyls using the same uptake coefficient for dicarbonyls (2.9×10^{-3}) as Li et al., (2013a), the contribution of SOA$_{het}$ to total SOA mass would increase to 72% (*i.e.*, 37% of SOA$_{het}$ formed from Gly; 35% of SOA$_{het}$ formed from Mgly) (Table S10 in the supplementary). However, this configuration may not reflect the real evolution of dicarbonyls, resulting in the underestimation on the dicarbonyls concentrations (i.e., the simulated concentration is at least one order of magnitude lower than the observation) (Figure S4) and overprediction of the contribution of SOA$_{het}$ to total SOA mass in this study (~51%).

   Table 3 compares the surface uptake coefficient derived from laboratory experiments and those used in different model simulation. It could be found that there was a large variation range for the surface uptake coefficients of Gly, while the studies on Mgly were still limited. For example, the laboratory experiment reported the surface uptake coefficients of Gly in the range of (0.8-6.6) and ($\leq 1 - 9$) $\times 10^{-3}$ on aqueous inorganic aerosols and cloud droplet/ice crystals, respectively (Volkamer et al., 2007; Loggio et al., 2005), and the coefficients were found to be $> 2.3 \times 10^{-3}$ for particles with high acidity (pH values within the range of -0.44 to -1.3) (Loggio et al., 2005). On

the other hand, Schweitzer et al. (1998) reported that the uptake coefficient of > 0.001 was only observed for lower temperature conditions, and the experimentally measured coefficient ranged from $(1.2 \pm 0.06) \times 10^{-2}$ to $(2.5 \pm 0.01) \times 10^{-3}$ on acidic solution (*i.e.*, 60-93 wt% H_2SO_4) at 253-273 k (Gomez et al., 2015; Zhang et al., 2015). It is suggested that more accurate and comprehensive parameterization of heterogeneous processes of dicabonyls still needs deeper exploration for further model development. The parameterization used in this study were mostly adopted from previous results, though it may still have limitations and uncertainties, the results of simulation at this site show better agreement with the observation.

Table 3 Surface uptake coefficient of Gly from laboratory experiments and used in the model simulation in the present and previous studies

Coefficient	References
$(0.8\text{-}7.3) \times 10^{-3}$, on aqueous inorganic aerosols	Volkamer et al., 2007; Loggio et al., 2005;
$(\leq 1 - 9) \times 10^{-3}$, and on cloud droplet/ice crystals	Volkamer et al., 2007; Loggio et al., 2005;
$(1.2 \pm 0.06) \times 10^{-2}$ - $(2.5 \pm 0.01) \times 10^{-3}$ on acidic solutions (*i.e.*, 60-93 wt% H_2SO_4 at 253-273 k)	Gomez et al., 2015; Zhang et al., 2015
3.3×10^{-3}	Knote et al., 2014 and references therein; Waxman et al., 2013; Waxman et al., 2013
2.9×10^{-3}	Fu et al., 2008
1.0×10^{-3}	Knote et al., 2014 and references therein; this study; Li et al., 2014

4. Conclusion

A photochemical box model coupled with MCM (v3.2) (PBM-MCM) and further improvements on the evolution of semi- and non-volatility oxidation products to a condensed particle-phase, was used to investigate the production and heterogeneous processes of Gly and Mgly, as well as the SOA-precursor relationship at a receptor site (*i.e.,* the Heshan site) for the first time in the PRD region. Compared to the measurements, the initial model configuration overestimated the Gly and Mgly concentrations by a factor of 3.3 and 3.5, respectively. This discrepancy occurred largely due to the absence of irreversible uptake and reversible partitioning. Model investigation regarding the production of Gly and Mgly revealed that the oxidation of

aromatics by OH radicals was the most important contributor to the formation of Gly and Mgly, with mean contributions of ~80% and ~94%, respectively, with toluene and *m,p*-xylene acting as the most important precursors for Gly and Mgly. For SOA formation, the heterogeneous processes of Gly and Mgly probably can explain ~21% of SOA mass in PRD. Toluene and *m,p*-xylene were the main precursors for SOA_{het} formation, while *o*-xylene was the most important precursor of SOA_{gp}. Overall, this study evaluated the formation and heterogeneous processes of Gly and Mgly in a polluted subtropical environment and highlighted the important role of intermediate products that are produced from photochemical oxidation of VOCs in SOA formation. The results of this study are expected to provide a better understanding of the evolution of VOC precursors, intermediate products, and heterogeneous process of the dicarbonyls, and the developed model modules can provide a robust tool for investigating SOA formation in the PRD and other regions in China.

References

Aumont, B., Valorso, R., Mouchel-Vallon, C., Camredon, M., Lee-Taylor, J., Madronich, S., 2012. Modeling SOA formation from the oxidation of intermediate volatility n-alkanes. Atmos. Chem. Phys. 12, 7577-7589.

Baum, E., 1997. Chemical property estimation: theory and application. Crc Press.

Benavent, N., Garcia-Nieto, D., Wang, S.S., Saiz-Lopez, A., 2019. Max-DOAS measurements and vertical profiles of glyoxal and formaldehyde in Madrid, Spain. Atmos. Environ. 199, 357-367.

Bienenstock, Y.S., 2001. Chamber studies of particulate production from hydroxyl reactions with toluene. M.Sc. thesis. York University, Toronto, Canada.

Bloss, C., Wagner, A., Bonzanini, M.E., Jenkin, K., Wirtz, K., Martin-Reviejo, M., Pilling, M.J., 2005. Evaluation of detailed aromatic mechanisms (MCMv3 and MCMv3.1) against environmental chamber data. Atmos. Chem. Phys. 5, 623e639.

Buxton, GeorgeáV, Malone, TreenaáN, áArthur Salmon, G. 1997. Oxidation of glyoxal initiated by OH in oxygenated aqueous solution. Journal of the Chemical Society, Faraday Transactions. 9316, 2889-2891.

Calvert, G., 2000. Evidence from functional magnetic resonance imaging of crossmodal binding in the human heteromodal cortex. Curr. Biol. 10(11), 649-657.

Calvert, J., Mellouki, A., Orlando, J., 2011. Mechanisms of atmospheric oxidation of the oxygenates. OUP USA.Carlton, A. G., Wiedinmyer, C., Kroll, J. H., 2009. A review of Secondary Organic Aerosol (SOA) formation from isoprene. Atmos. Chem. Phys. 9(14), 4987-5005.

Carlton, A. G., Wiedinmyer, C., Kroll, J. H., 2009. A review of Secondary Organic Aerosol (SOA) formation from isoprene. Atmos. Chem. Phys. 9(14), 4987-5005.

Chang, D., Wang, Z., Guo, J., Li, T., Liang, Y. H., Kang, L. Y., Xia, M., Wang, Y., Yu, C., Yun, H., Yue, D. L., Wang, T., 2019. Characterization of organic aerosols and their precursors in southern China during a severe haze episode in January 2017. Sci. Total Environ. 691, 101-111.

Corrigan, A. L., Hanley, S. W., De Haan, D. O., 2008. Uptake of glyoxal by organic and inorganic aerosol. Environ. Sci. Technol., 42, 4428−4433.

De Haan, D. O., Jimenez, N. G., De Loera, A., Cazaunau, M., Gratien, A., Pangui, E., 2018. Methylglyoxal Uptake Coefficients on Aqueous Aerosol Surfaces. J. Phys. Chem. A. 12221, 4854-4860.

De Haan, D.O., Corrigan, A.L., Tolbert, M.A., Jimenez, J.L., Wood, S.E., Turley, J.J., 2009. Secondary organic aerosol formation by sel-reactions of methylglyoxal and glyoxal in evaporating droplets. Environ. Sci. Technol. 43, 8184-8190.

Digangi, J.P. Henry, S.B., Kammrath, A., Boyle, E.S., Kaser, L., Schnizhofer, R., Graus, M., Turnipseed, A., Park, J-H., Weber, R.J., Hornbrook, R.S., Cantrell, C.A., Maudlin III, R.L., Kim, S., Nakashima, Y., Wolfe, G.M., Kajii, Y., Apel, E.C.,

Goldstein, A.H., Guenther, A., Karl, T., Hansel, A., Keutsch, F.N., 2012. Observations of glyoxal and formaldehyde as metrics for the anthropogenic impact on rural photochemistry. Atmos. Chem. Phys. 12, 9529-9543.

Ding, X., He, Q. F., Shen, R. Q., Yu, Q. Q., Wang, X. M., 2015. Spatial distributions of secondary organic aerosols from isoprene, monoterpenes,\r β\r -caryophyllene, and aromatics over China during summer. J. Geophys. Res. Atmos. 119(20), 11,877-11,891.

Ding, X., He, Q.F., Shen, R.Q., Yu, Q.Q., Zhang, Y.Q., Xin, J.Y., Wen, T.X., Wang, X.M., 2016. Spatial and seasonal variations of isoprene secondary organic aerosol in China: Significant impact of biomass burning during winter. Scientific Reports. 6, 20411.

Ding, X., Zhang, Y.Q., He, Q.F., Yu, Q.Q., Wang, J.Q., Shen, R.Q., Song, W., Wang, Y.S., Wang, X.M., 2017. Significant increase of aromatics-derived secondary organic aerosol during fall to winter in China. Environ. Sci. Technol. 51, 7432-7441.

Ervens, B. and Volkamer, R., 2010. Glyoxal processing by aerosol multiphase chemistry: towards a kinetic modeling framework of secondary organic aerosol formation in aqueous particles. Atmos. Chem. Phys. 1017, 8219-8244.

Ervens, B., Turpin, B. J., Weber, R. J., 2011. Secondary organic aerosol formation in cloud droplets and aqueous particles (aqSOA): a review of laboratory, field and model studies. Atmos. Chem. Phys. 1121, 22301-22383.

Fan, S. J., Fan, Q., Yu, W., Luo, X. Y., Wang, B. M., Song, L. L., Leong, K. L., 2011. Atmospheric boundary layer characteristics over the Pearl River Delta, China during summer 2006: measurement and model results. Atmos. Chem. Phys. 1113, 6297-6310.

Fick, J., Pommer, L., Nilsson, C., Andersson, B., 2003. Effect of OH radicals, relative humidity, and time on the composition of the products formed in the ozonolysis of α-pinene. Atmos. Environ. 3729, 4087-4096.

Friedfeld, S., Fraser, M., Ensor, K., Tribble, S., Rehle, D., Leleux, D. and Tittel, F., 2002. Statistical analysis of primary and secondary atmospheric formaldehyde. Atmos. Environ. 36(30), 4767-4775.

Fu, T.-M., Jacob, D.J., Wittrock, F., Burrows, J.P., Henze, D.K., 2008. Global budgets of atmospheric glyoxal and methylglyoxal, and implications for formation of secondary organic aerosols. J. Geophys. Res. Atmos. 113(D15).

Fu, T.-M., Cao, J.J., Zhang, X.Y., Lee, S.C., Zhang, Q., Han, Y.M., Qu, W.J., Han, Z., Zhang, R., Wang, Y.X., Chen, D., Henze, D.K., 2012. Carbonaceous aerosols in China: top-down constraints on primary sources and estimation of secondary contribution. Atmos. Chem. Phys. 12, 2725-2746.

Fuchs, H., Hofzumahaus, A., Rohrer, F., Bohn, B., Brauers, T., Dorn, H. P., Haseler, R., Holland, F., Kaminski, M., Li, X.,Lu, K., Nehr, S., Tillmann, R., Wegener, R., and Wahner, A., 2013. Experimental evidence for efficient hydroxyl radical regeneration in isoprene oxidation, Nat. Geosci., 6, 1023–1026.

Ge, Yu, Bayer, Amanda R, Galloway, Melissa M, Korshavn, Kyle J, Fry, Charles G, Keutsch, Frank N. 2011. Glyoxal in aqueous ammonium sulfate solutions:

849   products, kinetics and hydration effects. Environ. Sci. Technol. 4515, 6336-
850   6342.

851 Gomez, M.E., Lin, Y., Guo, S., Zhang, R., 2015. Heterogeneous chemistry of glyoxal
852   on acidic solutions. An oligomerization pathway for secondary organic aerosol
853   formation. J. Phys. Chem. A. 119, 19, 4457-4463.

854 Grosjean, D, Grosjean, E, Gertler, A., 2001. On-road emissions of carbonyls from light-
855   duty and heavy-duty vehicles. Environ. Sci. Technol. 351, 45-53.

856 Guo, S., Hu, M., Guo, Q., Zhang, X., Zheng, M., Zheng, J., Chang, C. C., Schauer, J.
857   J., Zhang, R., 2012. Primary sources and secondary formation of organic
858   aerosols in Beijing, China. Environ. Sci. Technol. 4618, 9846-9853.

859 He, L-Y., Huang, X.-F., Xue, L., Hu, M., Zheng, J., Zhang, R.Y., Zhang, Y.H., 2011.
860   Submicron aerosol analysis and organic source apportionment in an urban
861   atmosphere in Pearl River Delta of China using high-resolution aerosol mass
862   spectrometry. J. Geophys. Res. 116, D12304, dio:10.1029/2010JD014566.

863 Hofzumahaus, A., Rohrer, F., Lu, K.D., Bohn, B., Brauers, T., Chang, C.C., Fuchs, H.,
864   Holland, F., Kita, K., Kondo, Y., Li, X., Lou, S.R., Shao, M., Zeng, L., Wahner,
865   A., Zhang, Y.H., 2009. Amplified trace gas removal in the troposphere. Science
866   324, 1702-1704.

867 Hoyle, C. R., Myhre, G., Berntsen, T. K., Isaksen, I. S. A., 2009. Anthropogenic
868   influence on SOA and the resulting radiative forcing. Atmos. Chem. Phys. 9(8),
869   2715-2728.

870 Huang, R.J., Zhang, Y.L., Bozzetti, C., Ho, K.F., Cao, J.J., et al., 2014. High secondary
871   aerosol contribution to particulate pollution during haze events in China. Nature
872   514, 218-222.

873 Hu, J., Wang, P., Ying, Q., Zhang, H., Chen, J., Ge, X., Li, X., Jiang, J., Wang, S., Zhang,
874   J. and Zhao, Y., 2017. Modeling biogenic and anthropogenic secondary organic
875   aerosol in China. Atmos. Chem. Phy. 17(1), pp.77-92.

876 Hynes, R.G., Angove, D.E., Saunders, S.M., Harverd, V., Azzi, M., 2005. Evaluation of
877   two MCMv3.1 alkene mechanisms using indoor environmental chamber data.
878   Atmos. Environ. 39, 7251e7262.

879 Jimenez, J. L., Canagaratna, M. R., Donahue, N. M., Prevot, A. S., Zhang, Q., Kroll, J.
880   H., Decarlo, P. F., Allan, J. D., Coe, H., Ng, N. L., 2009. Evolution of organic
881   aerosols in the atmosphere. Science (New York, N.Y.). 326(5959), 1525-1529.

882 Johnson, D., Jenkin, M. E., Wirtz, K., Martin-Reviejo, M., 2004. Simulating the
883   formation of secondary organic aerosol from the photooxidation of toluene.
884   Environ. Chem. 1(3), 150-165.

885 Johnson, D., Jenkin, M. E., Wirtz, K., Martin-Reviejo, M., 2005. Simulating the
886   formation of secondary organic aerosol from the photooxidation of aromatic
887   hydrocarbons. Environ. Chem. 2(1), 35-48.

888 Johnson, D., Utembe, S. R., Jenkin, M. E., 2006. Simulating the detailed chemical
889   composition of secondary organic aerosol formed on a regional scale during the
890   TORCH 2003 campaign in the southern UK. Atmos. Chem. Phys. 6(2), 419-
891   431.

892 Kamens, R., Jang, M., Chien, C. J., Leach, K., 1999. Aerosol Formation from the

Reaction of α-Pinene and Ozone Using a Gas-Phase Kinetics-Aerosol Partitioning Model. Environ. Sci. Technol. 33(9), 1430-1438.

Kampf, C. J. , Waxman, E. M. , Slowik, J. G. , Dommen, J. , Pfaffenberger, L. , Praplan, A. P. , André SH, Baltensperger, U, Hoffmann, T, Volkamer, R., 2013. Effective Henry's law partitioning and the salting constant of glyoxal in aerosols containing sulfate. Environ. Sci. Technol. 47(9), 4236-4244.

Kanaya, Y., Cao, R., Akimoto, H., Fukuda, M., Komazaki, Y., Yokouchi, Y., Koike, M., Tanimoto, H., Takegawa, N., Kondo, Y., 2007. Urban photochemistry in central Tokyo: 1. Observed and modeled OH and HO2 radical concentrations during the winter and summer of 2004. J. Geophys. Res. Atmos. 112(D21).

Knote, C., Hodzic, A., Jimenez, JL, Volkamer, R., Orlando, JJ, Baidar, S, Brioude, J, Fast, J, Gentner, DR, Goldstein, AH. 2014. Simulation of semi-explicit mechanisms of SOA formation from glyoxal in aerosol in a 3-D model. Atmos. Chem. Phys. 1412, 6213-6239.

Kurtén, T., Elm, J., Prisle, N.L., Mikkelsen, K.V., Kampf, C.J., Waxman, E.M. Volkamer, R., 2014. Computational study of the effect of glyoxal–sulfate clustering on the Henry's law coefficient of glyoxal. J. Geophys. Res. Atmos. 119(19), 4509-4514.

Kroll, J. H., Ng, N. L., Murphy, S. M., Flagan, R. C., Seinfeld, J. H., 2005. Secondary organic aerosol formation from isoprene photooxidation under high-NOx conditions. Geophys. Res. Lett. 32(18).

Lam, S.H.M., Saunders, S.M., Guo, H., Ling, Z.H., Jiang, F., Wang, X.M. and Wang, T.J., 2013. Modelling VOC source impacts on high ozone episode days observed at a mountain summit in Hong Kong under the influence of mountain-valley breezes. Atmos. Environ. 81, 166-176.

Lee-Taylor, J., Madronich, S., Aumont, B., Baker, A., Camredon, M., Hodzic, A., Tyndall, G.S., Apel, E., Zaveri, R.A., 2011. Explicit modeling of organic chemistry and secondary organic aerosol partitioning for Mexico City and its outflow plume. Atmos. Chem. Phys. 11, 13219-13241.

Li, J., Cleveland, M., Ziemba, L. D., Griffin, R. J., Barsanti, K. C., Pankow, J. F., 2015. Modeling regional secondary organic aerosol using the Master Chemical Mechanism. Atmos. Environ. 102, 52-61.

Li, N., Fu, T. M., Cao, JJ., Lee, S., Huang, X. F., He, L. Y., Ho, K. F., Fu, J. S., Lam, Y. F,. 2013a. Sources of secondary organic aerosols in the Pearl River Delta region in fall: Contributions from the aqueous reactive uptake of dicarbonyls. Atmos. Environ. 763, 200-207.

Li, X., Brauers, T., Hofzumahaus, A., Lu, K., Li, Y. P., Shao, M., Wagner, T., Wahner, A., 2013b. MAX-DOAS measurements of NO2, HCHO and CHOCHO at a rural site in Southern China. Atmos. Chem. Phys. 13(4), 2133-2151.

Li, X., Rohrer, F., Brauers, T., Hofzumahaus, A., Wahner, A., 2014. Modeling of HCHO and CHOCHO at a semi-rural site in southern China during the PRIDE-PRD2006 campaign. Atmos. Chem. Phys. 14, 33013-33054.

Li, T., Wang, Z., Wang, Y.R., Wu, C., Liang, Y.H., Xia, M., Yu, C., Yun, H., Wang, W.H., Wang, Y., Guo, J., Herrmann, H., Wang, T., 2020. Chemical characteristics of

cloud water and impacts on aerosol properties at a subtropical mountain site in Hong Kong SAR. Atmos. Chem. Phys. 20, 391-407.

Li, Yang, Shao, Min, Lu, Sihua, Chang, Chih-Chung, Dasgupta, Purnendu K. 2010. Variations and sources of ambient formaldehyde for the 2008 Beijing Olympic games. Atmospheric Environment. 4421-22, 2632-2639.

Liggio, J., Li, S. M., Mclaren, R., 2005. Reactive uptake of glyoxal by particulate matter. J. Geophys. Res. Atmos. 110(D10).

Ling, Z. H., Guo, H., Lam, S. H. M., Saunders, S. M., Wang, T., 2014. Atmospheric photochemical reactivity and ozone production at two sites in Hong Kong: Application of a master chemical mechanism–photochemical box model. J. Geophys. Res. Atmos. 119(17), 10567-10582.

Ling, Z., Guo, H., Chen, G., Lam, S. H. M., Fan, S., 2016. Formaldehyde and acetaldehyde at different elevations in mountainous areas in Hong Kong. Aerosol Air Qual Res, 16(8), 1868-1878.

Ling, Z. H., He, Z. R., Wang, Z., Shao, M., Wang, X. M., 2019. Sources of methacrolein and methyl vinyl ketone and their contributions to methylglyoxal and formaldehyde at a receptor site in Pearl River Delta. J. Environ. Sci. 5, 1-10.

Liu, Y., Shao, M., Lu, S., Chang, C. C., Wang, J. L., Chen, G., 2007. Volatile Organic Compound (VOC) measurements in the Pearl River Delta (PRD) region, China. Atmos. Chem. Phys. 7(5), 1531-1545.

Lou, S., Holland, F., Rohrer, F., Lu, K., Bohn, B., Brauers, T., Chang, C. C., Fuchs, H., Häseler, R., Kita, K., Kondo, Y., Li, X., Shao, M., Zeng, L., Wahner, A., Zhang, Y., Wang, W., Hofzumahaus, A., 2010. Atmospheric OH reactivities in the Pearl River Delta – China in summer 2006: measurement and model results. Atmos. Chem. Phys. 1022, 11243-11260.

Lu, K. D., Hofzumahaus, A., Holland, F., Bohn, B., Brauers, T., Fuchs, H., Hu, M., Häseler, R., Kita, K., Kondo, Y., Li, X., Lou, S. R., Oebel, A., Shao, M., Zeng, L. M., Wahner, A., Zhu, T., Zhang, Y. H., Rohrer, F., 2013. Missing OH source in a suburban environment near Beijing: observed and modelled OH and HO 2 concentrations in summer 2006. Atmos. Chem. Phys. 13(2), 1057-1080.

Lv, S., Gong, D., Ding, Y., Lin, Y., Wang, H., Ding, H., 2019. Elevated levels of glyoxal and methylglyoxal at a remote mountain site in southern China: Prompt in-situ formation combined with strong regional transport. Sci. Total Environ. 672, 869-882.

Lyu, X. P., Chen, N., Guo, H., Zhang, W. H., Liu, M., 2015. Ambient volatile organic compounds and their effect on ozone production in Wuhan, central China. Sci. Total Environ. 541(60), 200-209.

Ma, X., Tan, Z., Lu, K., Yang, X., Liu, Y., Li, S., Li, X., Chen, S., Novelli, A., Cho, C., Zeng, L., 2019. Winter photochemistry in Beijing: Observation and model simulation of OH and HO2 radicals at an urban site. Sci. Total Environ. 685, 85-95.

Madronich, S., Flocke, S., 1997. Theoretical estimation of biologically effective UV radiation at the Earth's surface. Solar ultraviolet radiation.

Matsunaga, A., Ziemann, P. J. 2010. Gas-wall partitioning of organic compounds in a

Teflon film chamber and potential effects on reaction product and aerosol yield measurements. Aerosol Sci Technol. 44(10), 881-892.

Mellouki, A., Wallington, T.J., Chen, J., 2015. Atmospheric chemistry of oxygenated volatile organic compounds: impacts on air quality and climate. Chem. Rev. 10, 3984-4014.

McNeill, V. F. 2015. Aqueous Organic Chemistry in the Atmosphere: Sources and Chemical Processing of Organic Aerosols, Environ. Sci. Technol., 49, 1237–1244.

Nishino, N., Arey, J., Atkinson, R., 2010. Formation yields of glyoxal and methylglyoxal from the gas-phase OH radical-initiated reactions of toluene, xylenes, and trimethylbenzenes as a function of NO2 concentration. J. Phys. Chem. A. 114(37), 10140-10147.

Noziere, B., Dziedzic, P., Córdova, A., 2008. Products and kinetics of the liquid-phase reaction of glyoxal catalyzed by ammonium ions (NH4+). J. Phys. Chem. A. 113(1), 231-237.

Pye, H. O. T., Murphy, B. N., Xu, L. , Ng, N. L., Carlton, A. G., Guo, H., 2017. On the implications of aerosol liquid water and phase separation for organic aerosol mass. Atmos. Chem. Phys. 17(1), 343-369.

Ren, X., Brune, W.H., Mao, J., Mitchell, M.J., Lesher, R.L., Simpas, J.B., Metcalf, A.R., Schwab, J.J., Cai, C., Li, Y., Demerjian, K.L., 2006. Behavior of OH and HO2 in the winter atmosphere in New York City. Atmos. Environ. 40, 252-263.

Schweitzer, F., Magi, L., Mirabel, P., George, C. (1998). Uptake rate measurements of methanesulfonic acid and glyoxal by aqueous droplets. J. Phys. Chem. A. 102(3), 593-600.

Stavarakou, T., Müller, J.-F., De Smedt, I., Van Roozendael, M., Kanakidou, M., Vrekoussis, M., Wittrock, F., Richter, A., Burrows, J.P., 2009. The continental source of glyoxal estimated by the synergistic use of spaceborne measurements and inverse modelling. Atmos. Chem. Phys. 9, 8431-8446.

Stein, A., Woolley, H., Cooper, S. D., Fairburn, C. G., 1994. An Observational Study of Mothers with Eating Disorders and Their Infants. J. Child. Psychol. Psyc. 35(4), 733-748.

Steinfeld., Jeffrey, I., 1998. Atmospheric chemistry and physics: from air pollution to climate change. Sci. Policy. Sustain. Dev. 40(7), 26-26.

Stroud, C. A. , Makar, P. A. , Michelangeli, D. V. , Mozurkewich, M. , Hastie, D. R. , & Barbu, A. , et al. (2004). Simulating organic aerosol formation during the photooxidation of toluene/nox mixtures: comparing the equilibrium and kinetic assumption. Environ. Sci. Technol. 38(5), 1471-9.

Sumner, A. J., Woo, J. L., McNeill, V. F., 2014. Model Analysis of secondary organic aerosol formation by glyoxal in laboratory studies: The case for photoenhanced chemistry. Environ. Sci. Technol. 4820, 11919-11925.

Tan, Z., Lu, K., Hofzumahaus, A., Fuchs, H., Bohn, B., Holland, F., Liu, Y., Rohrer, F., Shao, M., Sun, K. and Wu, Y., 2019. Experimental budgets of OH, HO2, and RO2 radicals and implications for ozone formation in the Pearl River Delta in China 2014. Atmos. Chem. Phys, 19(10).

1025 Volkamer, R., Barnes, I., Platt, U., Molina, L. T., Molina, M. J., 2006. Remote sensing
1026   of glyoxal by differential optical absorption spectroscopy (DOAS):
1027   Advancements in simulation chamber and field experiments. Environmental
1028   Simulation Chambers: Application to Atmospheric Chemical Processes:
1029   Springer.
1030 Volkamer, R., San Martini, F., Molina, L. T., Salcedo, D., Jimenez, J. L., Molina, M. J.,
1031   2007. A missing sink for gas-phase glyoxal in Mexico City: Formation of
1032   secondary organic aerosol. Geophys. Res. Lett. 34(19), 255-268.
1033 Wang, B. L., Liu, Y., Shao, M., Lu, S. H., Wang, M., Yuan, B., 2016. The contributions
1034   of biomass burning to primary and secondary organics: A case study in Pearl
1035   River Delta (PRD), China. Sci. Total Environ. 569-570, 548-556.
1036 Wang, M., Zeng, L., Lu, S., Shao, M., Liu, X., Yu, X., 2014. Development and
1037   validation of a cryogen-free automatic gas chromatograph system (GC-MS/FID)
1038   for online measurements of volatile organic compounds. Anal. Methods. 6(23),
1039   9424-9434.
1040 Wang, S., Wu, D., Wang, X. M., Fung, J. C. H., Yu, J. Z., 2013. Relative contributions
1041   of secondary organic aerosol formation from toluene, xylenes, isoprene, and
1042   monoterpenes in Hong Kong and Guangzhou in the Pearl River Delta, China:
1043   an emission-based box modeling study. J. Geophys. Res. Atmos. 118, 507-519.
1044 Wang, X.M., 2019. Study on the roles of semi-volatile organic compound in the
1045   formation of secondary organic aerosol in East China. NSFC briefing in
1046   Guangzhou, China. Page 3.
1047 Wang, X.M., Wu, Z.Y., Liang, G.X., 2009. WRF/CHEM modeling of impacts of
1048   weather conditions modified by urban expansion on secondary organic aerosol
1049   formation over Pearl River Delta. Particuology 7, 384-391.
1050 Wang, Y., Wang, H., Guo, H., Lyu, X.P., Cheng, H.R., Ling, Z.H., Louie, P.K.K.,
1051   Simpson, I.J., Meinardi, S., Blake, D.R., 2017. Long-term O_3-precursor
1052   relationships in Hong Kong: field observation and model simulation. Atmos.
1053   Chem. Phys. 17, 10919-10935.
1054 Waxman, E. M., Elm, J., Kurtén, T., Mikkelsen, K. V., Ziemann, P. J., Volkamer, R.,
1055   2015. Glyoxal and methylglyoxal setschenow salting constants in sulfate,
1056   nitrate, and chloride solutions: Measurements and Gibbs energies. Environ. Sci.
1057   Technol. 4919, 11500-11508.
1058 Waxman, E.M., Dzepina, K., Erves, B., Lee-Taylor, J., Aumont, B., Jimenez, J.L.,
1059   Madronich, S., Volkamer, R., 2013. Secondary organic aerosol formation from
1060   semi- and intermediate volatility organic compounds and glyoxal: relevance of
1061   O/C as a tracer for aqueous multiphase chemistry. Geophys. Res. Lett. 40, 978-
1062   982.
1063 Washenfelder, R.A., Young, C.J., Brown, S.S., Angevine, W.M., Atlas, E.L., Blake,
1064   D.R., Bon, D.M., Cubison, M.J., De Gouw, J.A., Dusanter, S., Flynn, J., 2011.
1065   The glyoxal budget and its contribution to organic aerosol for Los Angeles,
1066   California, during CalNex 2010. J. Geophys. Res. Atmos. 116(D21).
1067 Wu, L.Q., Wang, X.M., Lu, S.H., Shao, M., Ling, Z.H., 2019. Emission inventory of
1068   semi-volatile and intermediate-volatility organic compounds and their effects

on secondary organic aerosol over the Pearl River Delta region. Atmos. Chem. Phys. 19, 8141-8161.

Xu, Z., Wang, T., Xue, L. K., Louie, P. K. K., Luk, C. W. Y., Gao, J., 2013. Evaluating the uncertainties of thermal catalytic conversion in measuring atmospheric nitrogen dioxide at four differently polluted sites in China. Atmos. Environ. 76(Sp. Iss. SI), 221-226.

Xue, L. K., Wang, T., Gao, J., Ding, A. J., Zhou, X. H., Blake, D. R., Wang, X. F., Saunders, S. M., Fan, S. J., Zuo, H. C., Zhang, Q. Z., Wang, W. X., 2014a. Ground-level ozone in four Chinese cities: precursors, regional transport and heterogeneous processes. Atmos. Chem. Phys. (14)23, 13175-13188.

Xue, L. K., Wang, T., Louie, P. K. K., Luk, C. W. Y., Blake, D. R., Xu, Z., 2014b. Increasing external effects negate local efforts to control ozone air pollution: a case study of Hong Kong and implications for other Chinese cities. Environ. Sci. Technol. 48(18), 10769-10775.

Ying, Q., Li, J., Kota, S. H.,2015. Significant contributions of isoprene to summertime secondary organic aerosol in eastern United States. Environ. Sci. Technol. 49(13), 7834-7842.

Yuan, B., Hu, W.W., Shao, M., Wang, M., Chen, W.T., Lu, S.H., Zeng, L.M., Hu, M., 2013. VOC emissions, evolutions and contributions to SOA formation at a receptor site in eastern China. Atmos. Chem. Phys. 13, 8815-8832.

Yun, H., Wang, W., Wang, T., Xia, M., Yu, C., Wang, Z., Poon, S. C. N., Yue, D., Zhou, Y., 2018. Nitrate formation from heterogeneous uptake of dinitrogen pentoxide during a severe winter haze in southern China. Atmos. Chem. Phys. 18(23), 17515-17527.

Zhang, X. and Seinfeld, J.H., 2013. A functional group oxidation model (FGOM) for SOA formation and aging. Atmos. Chem. Phys. 13, 5907-5926.

Zhang, X., Cappa, C. D., Jathar, S. H., McVay, R. C., Ensberg, J. J., Kleeman, M. J., Seinfeld, J. H. 2014. Influence of vapor wall loss in laboratory chambers on yields of secondary organic aerosol. Proceedings of the National Academy of Sciences. 111(16), 5802-5807.

Zhang, R.Y., Wang, G.H., Guo, S., Zamora, M.L., Ying, Q., Lin, Y., Wang, W.G., Hu, M., Wang, Y., 2015. Formation of urban fine particle matter. Chem. Rev. 115, 3803-3855.

Zhang, Y. L., Wang, X. M., Sheng, W., Herrmann, H., Yang, W. Q., Huang, X. Y., Zhou, Z., Huang, Z. H., He, Q. F., George, C., 2016. On-road vehicle emissions of glyoxal and methylglyoxal from tunnel tests in urban Guangzhou, China. Atmos. Environ. 127 55-60.

Zhang, Z., Wang, H., Chen, D., Li, Q., Thai, P., Gong, D., 2017. Emission characteristics of volatile organic compounds and their secondary organic aerosol formation potentials from a petroleum refinery in pearl river delta, china. Science of The Total Environment. Sci. Total Environ. 584-585, 1162.

Zhou, X., Mopper, K., 1990. Measurement of sub-parts-per-billion levels of carbonyl compounds in marine air by a simple cartridge trapping procedure followed by liquid chromatography. Environ. Sci. Technol. 24(10), 1482-1485.

1113 Zhou, Y, Zhong, LJ, Yue, DL, Zeng, LM, Zhang, T. 2014. Potential ozone formation
1114   and emission sources of atmospheric VOCs in Heshan during typical pollution
1115   episode. Environ. Monit. Forewarning. 6 1-5.

1116 Zhou, Y., Yue, DL, Zhong, LJ, Zeng, LM. 2013. Properties of atmospheric PAN
1117   pollution in Heshan during summer time. Admin. Tech. Environ. Monitor. 4 24-
1118   27.

1119 Zhu, T., Shang, J., Zhao, D. F., 2011. The roles of heterogeneous chemical processes in
1120   the formation of an air pollution complex and gray haze. Sci. China. Chem.
1121   54(1), 145-153.